Classification of Winter Sea Ice Types in Sentinel-1 SAR images

Jeong-Won Park[1,2], Anton A. Korosov[1], Mohamed Babiker[1], Joong-Sun Won[3], Morten W. Hansen[1,4], Hyun-cheol Kim[2]

[1]Ocean and Sea Ice Remote Sensing Group, Nansen Environmental and Remote Sensing Center, Bergen, 5006, Norway
[2]Unit of Arctic Sea Ice Prediction, Korea Polar Research Institute, Incheon, 21990, South Korea
[3]Department of Earth System Sciences, Yonsei University, Seoul, 03722, South Korea
[4]Department of Remote Sensing and Data Management, Norwegian Meteorolotical Institute, 0371 Oslo, Norway

Correspondence to: Jeong-Won Park (jeong-won.park@kopri.re.kr)

Abstract. A new Sentinel-1 image-based sea ice classification algorithm using a machine learning-based model trained in a semi-automated manner is proposed to support daily ice charting. Previous studies mostly rely on manual work in selecting training and validation data. We show that the readily available ice charts from the operational ice services can reduce the number of manual works in preparation of large amounts of training/testing data. Furthermore, they reduce the inconsistent decisions in the classification algorithm by indirectly exploiting the best ability of the sea ice experts working at the operational ice services. The proposed scheme has two phases: training and operational. Both phases start from the removal of thermal, scalloping, and textural noise from Sentinel-1 data and calculation of gray level co-occurrence matrix and Haralick texture features in a sliding window. In the training phase, the weekly ice charts are reprojected into the SAR image geometry. A random forest classifier is trained with the texture features on input and labels from the rasterized ice charts on output. Then, the trained classifier is directly applied to the texture features from Sentinel-1 images in an operational manner. Test results from the datasets spanning two winter seasons acquired over the Fram Strait and the Barents Sea showed that the classifier is capable of retrieving three generalized cover types (open water, mixed first-year ice, old ice) with an overall accuracy of 85% and five cover types (open water, new ice, young ice, first-year ice, old ice) with an accuracy of 58%. The errors are attributed both to incorrect manual classification on the ice charts and to the semi-automated algorithm. Finally, we demonstrate the potential for near-real time service of the ice map using daily mosaiced Sentinel-1 images.

1 Introduction

Wide swath SAR observation from several spaceborne SAR missions (RADARSAT-1, 1995-2013; Envisat ASAR, 2002-2012; ALOS-1 PALSAR, 2006-2011; RADARSAT-2, 2007-present; Sentinel-1, 2014-present) played an important role in studying global ocean and ice-covered Polar Regions. The Sentinel-1 constellation (1A and 1B) is producing dual-polarization observation data with the largest Arctic coverage and the highest temporal resolution ever. The cross-polarization is known to be more sensitive to the difference in scattering from sea ice and open water than the co-polarization (Scheuchl et al., 2004), and the combination of HH- and HV-polarizations has been widely used for ice edge detection and ice type classification.

However, most of the recent ice classification algorithms were developed using RADARSAT-2 ScanSAR (Leigh et al., 2014; Liu et al., 2015; Zakhvatkina et al., 2017) which has different sensor characteristics from Sentinel-1 TOPSAR, and the use of Sentinel-1 for the same purpose is very limited in literature. The main drawback of applying existing algorithms to Sentinel-1 TOPSAR data is the relatively high level of thermal noise contamination and its propagation to image textures.

For proper use of dense time-series of Earth observations using SAR sensors, radiometric properties must be well-calibrated. Thermal noise is often neglected in many cases, but is impacting seriously the utility of dual-polarization SAR data. Sentinel-1 TOPSAR image intensity is particularly disturbed by the thermal noise in the cross-polarization channel. Although the European Space Agency (ESA) provides calibrated noise vectors for noise power subtraction, residual noise contribution is still significant considering the relatively narrow backscattering distribution of the cross-polarization channel. In our previous study (Park et al. 2018), a new denoising method with azimuth de-scalloping, noise scaling, and inter-swath power balancing was developed and showed improved performance in various SAR intensity-based applications. Furthermore, when it came to texture-based image classification, we suggested a correction method for textural noise (Park et al., 2019) which distorts local statistics thus degrades texture information in the Sentinel-1 TOPSAR images.

In many of the previous works on ice-water and/or sea ice classification (Soh and Tsatsoulis, 1999; Zakhvatkina et al., 2013; Leigh et al., 2014; Liu et al., 2015; Ressel et al., 2015; Zakhvatkina et al., 2017; Aldenhoff et al., 2018), the training and validation were done using manually produced ice maps. Although the authors claimed that the manual ice maps were drawn by ice experts, the selection of SAR scenes and interpretation can be inconsistent, and the number of samples was not enough to generalize the results because of the laborious manual work. Therefore, increasing objectivity is crucial, and automating the classification process is encouraged. The idea of training using SAR images and accompanying image analysis charts, which is a raw interpretation of SAR images by trained ice analysts working at operational ice services, were tested for sea ice concentration estimation by Wang et al. (2017); however, such image analysis charts are not accessible to the public.

The use of a public ice chart as training and validation reference data may help in solving the validation problem and enabling automation. The preparation of a public ice chart is also through manual inspection of various sources of satellite imagery and other sources of data (Partington et al., 2003; Johannessen et al., 2006); however, training using a large volume of these charts would reduce operator-to-operator bias. The overall bias may exist since the public ice charts are produced in the interest of marine safety. Nevertheless, as the human interpretation available in the ice chart is currently considered as the best available information of sea ice (Karvonen et al., 2015), the best practice to make a sea ice type classifier is to train with the public ice chart so that the best knowledge of certified ice analysts is mimicked.

In this work, we present a semi-automated Sentinel-1 image-based sea ice classification algorithm which takes advantage of our denoising method. The noise corrected dual-polarization images are processed into image textures that capture sea ice features in various spatial scales, and they are used for supervised classification with a random forest classifier by relating with ice charts published by operational ice services. The use of ice charts has dual purposes: semi-automatization of classifier training, and minimization of human error.

2 Data and methods

2.1 Study area and used data

The region of study for developing and testing the proposed algorithm is the Fram Strait and the Barents Sea including a part of the Arctic Ocean (10ºW-70ºE, 75ºN-85ºN) as shown in Figure 1. Various sea ice types are found in this area due to the intensive export of multi-year ice through the Fram Strait (Smedsrud et al., 2017), and development of young and first-year ice between Svalbard and Franz Josef Land.

Sentinel-1 TOPSAR data in Extended Wide-swath (EW) mode acquired in two winter seasons (Dec. 2017 – Mar. 2018 and Dec. 2018 – Mar. 2019) were collected from the Copernicus Open Access Hub (https://scihub.copernicus.eu). The number of daily image acquisitions covering the study area ranges from 6 to 10 depending on the orbits. The images from the first year (hereafter called 2018 data) are used to train the classifier and those from the second year (hereafter called 2019 data) are used for validation.

The ice charts covering the same periods were collected. There are two ice services that publish weekly ice charts with Pan-Arctic coverage: U. S. National Ice Center (NIC) of the United States of America, and Arctic and Antarctic Research Institute (AARI) of Russia. Although the accuracies are known to be comparable (Pastusiak, 2016) to each other, there is no partial ice concentration information in the AARI ice chart. In this study, we use the ice charts downloaded from the NIC website (https://www.natice.noaa.gov/Main_Products.htm).

2.2 Methods

Figure 2 shows the flow of the semi-automated ice classification scheme that we propose. It is divided into two phases: training and operational. Both phases start from the removal of thermal noise from Sentinel-1 data (Section 2.2.2), incidence angle calibration (Section 2.2.3), and calculating texture features (Section 2.2.4). The training phase (shown in gray in Figure 2) continues with preprocessing and collocation of the ice charts with the Sentinel-1 data (Section 2.2.1) and machine learning step (Section 2.2.5 and 2.2.6). The operational phase uses the classifier of which developed during the training phase for processing texture features that were computed from the input SAR data and for generating ice charts. Detailed explanations for each step are given in the following subsections.

2.2.1 Ice chart preprocessing

To take advantage of the objective identification of the ice type and to develop a semi-automated processing scheme, the proposed algorithm uses electronic ice charts published by international ice chart services. The electronic ice chart follows SIGRID-3 format (JCOMM, 2014a), which is based on a vector format called shapefile (ESRI, 1998). The first step is to reproject the ice chart into the geometry of each SAR image. Although an accurate reprojection needs several pieces of information such as orbit, look angle, topographic height, etc., our interest is in the sea ice where the topographic difference does not exceed more than few meters, hence the reprojection of coordinates of ice chart polygons is done with Geospatial

Data Abstraction Library (GDAL; GDAL/OGR contributors, 2019) using a simple 3rd order polynomial fitted using the ground control points information from the Sentinel-1 product-included auxiliary data.

After the reprojection, the following three layers are extracted: total ice concentration (CT), partial ice concentration of each ice type (CP), and stage of development (SoD). CT is important because areas with low CT can be misinterpreted as open ocean in a SAR image. Heinrichs et al. (2006) reported that the ice edge determined from AMSR-E passive microwave radiometer data using the isoline of 15% concentration matches best the ice edge determined from RADARSAT-1 SAR data using visual inspection. After the visual comparison of many SAR images and the corresponding reprojected ice charts, we set a threshold of 20% for CT to discard water-like pixels. Note that the ice concentration label in the SIGRID-3 format is assigned in an increment of 10%. CP is also important in finding the dominant ice type in the given polygons. SoD is a so-called ice type. It is challenging to differentiate ice types using SAR data only, thus we merged the SoDs into simple five classes: open water, new ice, young ice, first-year ice, and old ice.

Figure 3 demonstrates an example of the ice chart preprocessing explained above with the colors following the WMO nomenclature (JCOMM, 2014b). Comparing the original SoD in the top left panel with the processed SoD in the bottom left panel, it is clear that the ice edge of the processed SoD match better with the SAR backscattering images.

2.2.2 Denoising of Sentinel-1 imagery

Sentinel-1 cross-polarization images suffer from strong noise of which are originated from combined effects of the relatively low signal-to-noise ratio of the sensor system and insufficient noise vector information in the Extra Wide-swath mode Level-1 product (Park et al., 2018). For surfaces with low backscattering such as calm open water and level sea ice without the presence of frost flowers on top, the effects from thermal noise contamination are visible not only in the backscattering image but also in some of the texture images (Park et al., 2019). The authors have developed an efficient method for textural denoising which is essential for the preprocessing of Sentinel-1 TOPSAR dual polarization products. Denoising ensures beam-normalized texture properties for all subswaths, which helps seamless mosaic of multi-pass images regardless of the satellite orbit and image acquisition geometry. By following the methods developed in Park et al. (2018, 2019), each of the Sentinel-1 images was denoised before further processes are applied.

2.2.3 Incidence angle correction

It is well known that there is a strong incidence angle dependence in the SAR backscattering intensity for open water and sea ice surface (Mäkynen et al., 2002; Mäkynen and Karvonen, 2017). For wide-swath SAR system like Sentinel-1 TOPSAR, varying backscatter intensity confuses image interpretation. The quasi-linear slopes in the plane of incidence angle versus sigma nought in decibel scale for typical first-year ice are reported as -0.24 and -0.16 dB/degree for HH- and HV-polarization, respectively (Mäkynen and Karvonen, 2017). To normalize the backscattering intensity for all swath range, these slopes were compensated for or used as input layer in several ice classification algorithms in the literature (Liu et al., 2015; Zakhvatkina et al., 2013, 2017; Karvonen, 2014, 2017; Aldenhoff et al., 2018). Although the angular dependency is not a system-dependent

variable but is governed by physical characteristics of the backscattered surface, the numbers need to be reassessed because the estimations of Mäkynen and Karvonen (2017) might have been affected by the residual thermal noise which used to be very strong before the ESA has updated the noise removal scheme in 2018 (Miranda, 2018).

Figure 4 shows two-dimensional histograms of incidence angle versus sigma nought for sea ice pixels in HH and HV polarization channels from Sentinel-1 data collected over sea ice and open water in the study area in winter 2018. From the Sentinel-1 dataset described in Section 2.1, sea ice pixels were extracted by using daily global sea ice edge products available from the EUMETSAT Ocean and Sea Ice Satellite Application Facilities (OSISAF). For HH polarization, the estimated slope was -0.200 dB/degree, which is slightly different from the estimation of the first-year ice (-0.24 dB/degree) in Mäkynen and Karvonen (2017) and in between the estimations for first-year ice (-0.22 dB/degree) and multi-year ice (-0.16 dB/degree) in Mahmud et al. (2018). For HV polarization, the estimated slope was only -0.025 dB/degree, which is much lower than the estimation in Mäkynen and Karvonen (2017), however, it is in line with the estimations from RADARSAT-2 (Leigh et al., 2014; Liu et al., 2015). We compensate for the incidence angle dependence using the estimated slopes with respect to the nominal scene center angle of 34.5 degrees as reference. Although the incidence angle dependence changes with ice type and radar frequency (Mahmud et al., 2018), the compensation is done for all pixels in the image using a single value of mean slope because the ice types are not identified in this stage. Open water areas of the image are also affected; however, the correction is also beneficial since the incidence angle dependence for open water is stronger (-0.65 dB/degree for wind velocity of 5 m/s, computed from CMOD5 C-band geophysical model function in Hersbach et al., 2007), thus the corrected image has less incidence angle dependence.

2.2.4 Texture feature computation

Like many of the previously developed sea ice type classification methods (Shokr, 1991; Barber and LeDrew, 1991; Soh and Tsatsoulis, 1999; Deng and Clausi, 2005; Zakhvatkina et al., 2013; Leigh et al., 2014; Liu et al., 2015), the proposed approach starts from gray level co-occurrence matrices (GLCM) calculation. The GLCM is a four-dimensional matrix $P(i, j, d, a)$ calculated from two grey tones of reference pixel i, and its neighbor j, with co-occurrence distance d, and orientation a. Haralick et al. (1973) have introduced a set of GLCM-based texture features called Haralick features, and its practicality has been reported in numerous research. Since 13 Haralick features can be calculated for each of the two-dimensional slices $P(i, j)$ for multiple d and a, the maximum number of texture features is to be as $2 \times 13 \times d \times a = 26da$, where 2 is for accounting dual polarization. It is common to take the directional average for 0°, 45°, 90°, and 135° to reduce GLCM dimensionality. Further averaging for multiple distances (1 to $w/2$ where w is the size of subwindow for GLCM computation) is taken after computing normalized GLCM. The spatial resolution of the texture features is the pixel spacing of Sentinel-1 EW-mode GRDM image (40 m) multiplied by w. In this study, we set w as 25 so that the grid spacing of the result of texture analysis is 1 km.

An important factor that influences the computed texture features is the number of gray levels, L. Considering the radiometric stability of Sentinel-1 EW mode (0.32 dB; Miranda, 2018) and the range of sigma nought for various ice types (-31 to 0 dB

for HH, -32 to -7 dB for HV; estimated from Figure 4 after incidence angle correction), the number of gray level should be sufficiently large enough to capture their actual differences in sigma nought values. The optimal quantization level can be calculated using the ratio of sigma nought range to radiometric resolution as follows:

For HH, $$\frac{(0\ dB)-(-31\ dB)}{0.32\ dB} = 96.875 \quad (1)$$

For HV, $$\frac{(-7\ dB)-(-32\ dB)}{0.32\ dB} = 78.125 \quad (2)$$

Since L should be sufficiently large to take the full advantage of system capability and yet, the computation cost should not be too expensive, in this study, we set L as 64, which is the closest power of 2 to the resulting numbers from the equations above. In addition to 13 Haralick features, the coefficient of variation (CV) which is reported as a useful feature for ice-water discrimination (Keller et al., 2017) is included. The CV is defined as follows:

$$CV = \sigma/\mu \quad (3)$$

where σ and μ are the standard deviation and mean of the samples in a given subwindow. Since CV can be computed for each polarization images, the number of texture features for Sentinel-1 dual-polarization data is extended to 28. Incidence angle and day-of-the-year can also be added. The former is adopted to account for possible residuals from the angular dependency correction while the latter is to account for seasonal variability. Although these two are not any type of textures, they can be used as input features for image classification. Note that it is important to have each ice type spatially and temporally even distributions if these two additional features are included; otherwise, the trained classifier will result a biased prediction. The effects of including these extra features will be tested and discussed in later sections.

2.2.5 Machine learning classifier

Since there are hundreds of algorithms in the field of machine learning (ML) and each of the different algorithms has its own pros and cons, it is not easy to compare their performances and decide what to use. Fernández-Delgado et al. (2014) evaluated that the Random Forest (RF; Ho, 1998) was the best classifier for various types of datasets with slight difference from Support Vector Machine (SVM; Cortes and Vapnik, 1995). In the literatures about sea ice classification, the SVM was used often because by nature it works relatively well even when the number of datasets are small. When training dataset is prepared by manual work (i.e., manual classification by human expert), the number of images is not large, usually less than 20 (e.g., 12 scenes in Zakhvatkina et al., 2013; 20 scenes in Leigh et al., 2013; 2 scenes in Liu et al., 2015; 4 scenes in Ressel et al., 2015). However, the number can increase with less effort when the readily available ice charts are used as training references. Besides, there is no need to rely on additional manual work prone to contamination by biased decisions. The RF has two practical advantages when processing a large number of datasets. First, the RF is scale-invariant and does not require preprocessing of

the datasets whereas the SVM requires scaling and normalization. Second, the computational complexity of the RF is lower than that of the SVM. For the SVM, the number of operations is $O(n^2p + n^3)$ and $O(n_{sv}p)$ for training and prediction while for RF, $O(n^2pn_{tr})$ and $O(n_{tr}p)$, respectively, where n is the number of samples, p is the number of features, n_{sv} for the number of support vectors, and n_{tr} for the number of trees. Considering the practical requirements of fast processing for near-real time ice charting services, the RF can be a reasonable solution. We use the RF with the Python Scikit-Learn implementation (Pedregosa et al., 2011).

We split the RF classifier into several binary classifiers using a one-vs-all scheme (Anand et al., 1995). Although the standard RF algorithm can inherently deal with a multiclass problem, the one-vs-all binarization to the RF results in better accuracy with smaller forest sizes than the standard RF (Adnan and Islam, 2015).

Three hyperparameters of the RF classifier were tuned: number of trees (N_T), maximum tree depth (D), and maximum number of features (N_F). Usually, with the higher N_T and D, the model better fits to the data. However, increasing forest size can slow down the training process considerably, and more importantly, it can cause overfitting. Therefore, it is important to tune these hyperparameters adequately so that the processing time and performance are in balance. To determine the best values of the hyperparameters, a grid search with five-fold cross-validation (Kohavi, 1995) is used. The grid (all possible combinations of N_T, D, and N_F values) is set in a logarithmic scale (Table 1) because the performance change with hyperparameter is typically in a logarithmic scale. Classification scores with values ranging from 0 (worst performance) to 1 (best performance) are evaluated for each node of the grid and are interpolated between the nodes by curve fitting. The Richards' Curve (Richards, 1959) was used as the fit model because it allows easy estimation of the model's maximum value. The optimal values for N_T, D, and N_F are selected based on the saturation of score increment, difference between training and testing score, and computational load considerations.

2.2.6 Training and validation

To train an ice type classifier, a set of collocated SAR images and ice charts is required. After the preprocessing of the ice chart including reprojection into the SAR image geometry, only the samples with spatially and temporally good matches should be fed to the training phase. Image selection is trivial, but not easy to automate. Since the weekly ice chart is made partly based on the SAR images acquired in the past three days from the date of publication, the ice edges in some images match well with those in the ice chart.

In order to automate image selection, the ice edges in SAR images need to be identified first. Since even an ice/water classifier has not been well developed yet for Sentinel-1, the image selection procedure has to be done manually in the beginning. However, once a classifier is generated with high accuracy, it can be used to automate the procedure, then the whole process in the proposed scheme will be fully automated. This is why the proposed algorithm is named "semi-" automated for now. Nevertheless, the manual selection is done by visual inspection of ice-water boundaries overlaid on SAR images. The ice-water boundary can be extracted easily from the reprojected ice chart by selecting the pixel borders of open water class. Then

the SAR backscattering image contrasts across the ice-water boundaries are examined both in HH- and HV-polarization because the image contrast between ice-water is larger in HV and smooth level ice is better recognizable in HH.

After the image selection, the samples in the selected images are split randomly into training and test datasets with a ratio of 7:3. For the training dataset, further data selection is made by excluding the samples residing close to the polygon boundaries. This is to account for possible mismatch due to various reasons (e.g., ice drift, vector mapping error, image geocoding error, etc.). In this study, only the data from pixels more than 3 km away from the polygon boundaries was fed into the training process. Once the hyperparameter optimization is done, the RF classifier is trained for the training dataset. The trained classifier is then applied to the test dataset. For performance evaluation, we use confusion matrix and Cohen's kappa coefficient κ (Cohen, 1960), which measures the agreement between two raters (in this study, they are the trained classifier and the reference ice chart) with taking account of the possibility of the agreement occurring by chance. The validation is done in the same way but using a completely independent dataset. The 2018 data was used to run the training phase. Among 958 images in total, we selected 57 images of which ice edges match well with the collocated ice chart. From the selected images, 6.4 million samples covering open water and sea ice were divided into training and test dataset.

3 Results and discussion

We trained three RF classifiers with different feature configurations: i) FC1: Haralick texture features and CV, ii) FC2: Haralick texture features, CV, and incidence angle, iii) FC3: Haralick texture features, CV, incidence angle, and day-of-the-year.

As expected, the classification score increases with the number of trees (crosses on Figure 5, upper panel) and Richards' curve (dashed line) fits well to the observations (RMSE=2.3×10^{-4}). The optimal N_T value is selected where the score increment per tree (i.e., local slope) becomes less than 0.001 (i.e., accuracy increase of 0.1%) and constitutes 11 trees thus keeping the forest size small. The scores also increase with the maximum tree depth (crosses on Figure 5, middle panel) but Richards' curve (dashed line) doesn't fit so well (RMSE=3.6×10^{-3}) and cannot be used for finding the optimal D value. This can be explained by overfitting of the classifier and illustrated by the difference between training and testing scores (Figure 5, lower panel): small difference between the scores (for $D \leq 8$) indicate similar performance on training and testing datasets, while large difference (for $D > 8$) indicate that testing dataset is processed with worse results. The optimal D value is therefore selected where the score difference become higher than 0.03 and constitutes 8 levels. The optimal value of the number of features (N_F) was selected using the same criterion as for N_T and the value constitutes 10 features. As a result, the optimal hyperparameters of the number of trees, the maximum tree depth, and the number of features were 11, 8, and 10, respectively.

The trained five-class classifier consists of five binary sub-classifiers, each of them is used for discriminating one specific class from the others. For each sub-classifier, each texture feature has a different weight in decision making. The fraction of the samples that each texture feature contributes can be used to compute the relative importance of the features, and the averaged estimates of them over several randomized trees serve as an indicator of feature importance (Louppe, 2014). The

feature importance of the sub-classifiers is presented in Figure 6. The overall pattern shows that the features of HV polarization play a more important role than those of HH polarization. For HH polarization, the sum average, which is equal to the mean backscattering intensity in each subwindow, was the prominent feature. For HV polarization, however, variance- and entropy-related features were more important. The classifiers for open water and old ice have more strong dependencies on HV polarization than others. This is understandable because the main radar scattering mechanisms for those two types are strongly characterized by the portion of volume scattering: low for calm water and high for dry ice with low salinity (old ice). The classifier for new ice has a distinctive pattern that the sum averages in both polarizations are much more important than other features. This might be because the new ice has different types of recently formed ice including nilas, which is smooth but rafting can make rough features, and frost flowers, which introduces high surface roughness and volume scattering (Isleifson et al., 2014), thus the new ice can appear either featureless dark or complex bright in SAR image (Dierking, 2010). The large range in backscatter values makes it hard to define characteristic texture in the new ice patch.

The confusion matrix for testing the trained classifier with the test dataset (2018 data) is shown is in Table 2. Three cases with different feature configurations (FC1-FC3) were tested. The accuracies for open water and old ice were higher than 85%; however, those for young ice and first-year ice were around 60%. The mean difference between the results of FC1 and FC2 was only 1.6%, indicating that residual angular dependency was negligible after the incidence angle correction. However, the accuracy significantly improved from FC2 to FC3, especially with new ice (24.5%). κ for FC1, FC2, and FC3 were 0.70, 0.71, and 0.77, respectively. It should be noted that the evaluation of the 2018 data was carried out with the input dataset that was used for training. Thus, the test and training data share the same ice conditions as well as spatio-temporal coverage. As a result, κ might contain correlation which is not preferable for proper evaluation. Table 3 shows the confusion matrix for validation results from the 2019 data of which the accuracy of open water and old ice was at a similar level, compared to the 2018 data. Meanwhile, for the accuracy of new ice, young ice, and first-year ice decreased considerably. The differences between the results of FC1 and FC2 were insignificantwhereas there were notable accuracy degrades from FC2 to FC3. This result is opposite to the 2018 data inferring that the training with FC3 was overfitted and the day-of-the-year may not correspond to the temperature, air-sea fluxes, or weather regimes. κ for FC1, FC2, and FC3 with the 2019 data were 0.67, 0.67, and 0.49, respectively.

To see how the denoising step in Section 2.2.2 led to improvements in the classification accuracies, the same training and evaluation were conducted for the same dataset without applying the textural noise correction (Table 4). In both FC1 and FC2, the accuracies improved for young ice (+8.2-9.8%) and first-year ice (+9.2-11.6%) which were most pronounced compared to those for open water (+1.7%) and old ice (+1.2-1.7%). On the contrary, a small accuracy decrease was observed for new ice (-2.8-4.7%). Nevertheless, the improvement in kappa (+0.05) demonstrates a clear improvement in the overall classification result.

Figure 7 shows a daily mosaic of Sentinel-1 SAR images over the study area and the classified ice map. For comparison, the NIC weekly ice chart is also displayed. Despite the SAR images had been acquired three days before the ice chart was published, the ice edges of the ice chart match well with the SAR mosaic in most parts because the same SAR data were used.

In overall, the discriminations between ice and non-ice, old ice and other ice types, and detection of new ice patches look reasonable. However, some young ice patches, for example the ice patches between the Svalbard archipelago, are misclassified as the first-year ice. Figure 8 shows another daily mosaic made by the images acquired on the same day of the ice chart publication. Considering notable ice drift in the backscattering images in Figure 7 and 8the SAR-based ice classification results in both figures look consistent, well in line with the ice drift. Although the weekly ice chart is supposed to represent the averaged ice status in the past few days, the actual ice distribution on the actual date of the publication can be largely different. This example shows a clear potential of near-real time service of ice type classification.

To cope with the ambiguous classification for the ice types with low accuracy, we conducted a test with the further simplification of ice types by combining the new ice, young ice, and first-year ice into the "mixed" first-year ice, and then training new classifiers. Table 5 and 6 show the confusion matrices for the three-class classifiers. κ for FC1, FC2, and FC3 were 0.84, 0.86, and 0.92 in 2018 data, and 0.80, 0.80, and 0.53 in 2019 data, respectively. The dramatic increase in the accuracy of the mixed first-year ice indicates that the misclassification for the new ice, young ice, and first-year ice was mostly among themselves. However, the accuracy decrease from 2018 data to 2019 data was at a similar level to the case of the five-class classification. This could have been caused by inconsistent labeling in the reference ice chart.

Figure 9 shows an example of the inconsistent labeling in the reference ice chart. The SoDs from the NIC ice charts are superimposed on the Sentinel-1 backscattering images. The same ice floe (red outline) is classified differently in two different ice charts (old ice on the left panel and first-year ice on the right panel) although it looks almost the same in the corresponding SAR backscattering images. It should be noted that training with ice chart might have included mislabeled small features even if the image selection based on ice edge matching was successful. Furthermore, the boundaries between different ice types in the ice chart are normally not as precise as those in the SAR image-based classification results. Therefore, the lower classification accuracies compared to those in the previous studies (80% in Zakhvatkina et al., 2013; 91.7% in Liu et al., 2015; 87.2% in Aldenhoff et al., 2018), which used manually classified ice maps as training and validation reference, are expected.

Unfortunately, the proposed algorithm has several limitations. First of all, the variations in radar backscattering and its corresponding image textures due to seasonal changes were not properly captured. Although day-of-the-year was tested as a seasonality variable in the FC3 feature configuration, the result did not show any improvement. This is because day-of-the-year might not correspond to the same temperature, fluxes, and weather regimes. Second, the proposed method struggles when the same sea ice is located on different marginal sides of SAR images because the incidence angle dependence could not be normalized perfectly. An example of such a failure can be seen along the image boundaries at 80N, 35E and 82.5N, 60E, approximately. Third, some artifacts were observed under an extreme marine condition. In the classified results in the bottom right panel of Figure 8, there is a misclassified FYI patch (yellow) in the open water area. According to the NOAA SAR wind image service, ANSWRS 2.0, the wind speed ranged from 17 to 21 m/s at the time of image acquisition heavily roughing the water surface.

4 Conclusion

A new semi-automated SAR-based sea ice type classification scheme was proposed in this study. For the first time several ice types can be successfully identified on Sentinel-1 SAR imagery. The main technological innovation is two-fold: i) minimized manual work in the preparation of training and validation reference data and ii) more objective evaluation of the SAR-based sea ice type classifier. A conventional approach for selecting training/testing data by anonymous human ice expert is undesirable not only because it is laborious, but also due to subjectivity and lack of standardization in the assessment of the automated classifier. Therefore, the performance from different literature sources cannot be intercompared directly.

Test results from the datasets of two winter seasons acquired over the Fram Strait and the Barents Sea area showed overall accuracies of 85% and 58% and κ of 0.80 and 0.67 for the three-class and five-class ice type classifiers, respectively. These are slightly lower than the numbers in the previous studies, and the errors are attributed not only to the automated algorithm but also to the inconsistency of the ice charts and the high level of their generalization. Based on the results, we envisage that three-class ice type classification from SAR imagery would be useful for making a global sea ice type product like EUMETSAT OSI-403-C (Aaboe et al., 2014) with higher spatial resolution. The proposed approach importantly showed that a daily ice type mapping from the Sentinel-1 data is feasible and can help capture details of short-term changes in the stage of sea ice development. Based on the achieved results, we believe that the proposed approach may be efficiently used for operational ice charting services for supporting navigation in the Arctic.

Code/Data availability

Not applicable

Author contributions

JP and AK formulated the research plan, JP and AK developed the algorithm, JP implemented the algorithm and performed the data processing, JP, AK, MB, JW, MH, and HK carried out the analyses, and JP wrote the paper.

Competing interests

The authors declare that they have no conflict of interests.

Financial support

This work was supported by the French Service Hydrographique et Océanographique de la Marine (SHOM) under SHOM-ImpSIM Project 111222, the Research Council of Norway and the Russian Foundation for Basic Research under NORRUSS Project 243608, SONARC, and the Korea Polar Research Institute under grant number PE20080.

References

Aaboe, S., Breivik, L.-A., and Eastwood, S.: Improvement of OSI SAF product of sea ice edge and sea ice type. EUMETSAT Meteorological Satellite Conference, Geneva (Switzerland), 22-26 September 2014.

Adnan, M. N., and Islam, M. Z., One-Vs-All Binarization Technique in the Context of Random Forest, Proc. European Symposium on Artificial Neural Networks, Computational Intelligence and Machine Learning, Bruges (Belgium), 22-24 April 2015.

Aldenhoff, W., Heuzé, C., and Eriksson, L.: Comparison of ice/water classification in Fram Strait from C- and L-band SAR imagery. Ann. Glaciol., 59(76pt2), 112-123. doi:10.1017/aog.2018.7, 2018.

Anand, R., Mehrotra, K., Mohan, C. K., and Ranka, S.: Efficient classification for multiclass problems using modular neural networks, IEEE T. Neural Networ., 6(1), 117-124, doi:10.1109/72.363444, 1995.

Barber, D. G. and LeDrew, E. F.: SAR sea ice discrimination using texture statistics: A multivariate approach. Photogramm. E. Rem. S., 57(4), 385-395, 1991.

Cohen, J.: A coefficient of agreement for nominal scales, Educ. Psychol. Meas., 20(1), 37–46, doi:10.1177/001316446002000104, 1960.

Cortes, C. and Vapnik, V.: Support-vector networks, Mach. Learn., 20(3), 273-297, doi: 10.1007/BF00994018, 1995.

Deng, H. and Clausi, D. A.: Unsupervised segmentation of synthetic aperture radar sea ice imagery using a novel Markov random field model," IEEE T. Geosci. Remote, 43(3), 528-538, doi:10.1109/TGRS.2004.839589, 2005.

Dierking, W.: Mapping of different sea ice regimes using images from Sentinel-1 and ALOS synthetic aperture radar, IEEE T. Geosci. Remote, 48(3), 1045-1058, doi:10.1109/TGRS.2009.2031806, 2010.

ESRI (Environmental Systems Research Institute, Inc.): ESRI Shapefile Technical Description, An ESRI White Paper, 1998. Available at: http://downloads.esri.com/support/whitepapers/mo_/shapefile.pdf

Fernández-Delgado, M., Cernadas, E., Barro, S., and Amorim, D.: Do we need hundreds of classifiers to solve real world classification problems?, J. Mach. Learn. Res., 15, 3133-3181, 2014.

GDAL/OGR contributors: GDAL/OGR Geospatial Data Abstraction software Library, Open Source Geospatial Foundation, 2019. URL https://gdal.org

Haralick, R. M., Shanmugam, K., Dinstein, I.: Textural features for image classification, IEEE T. SYST. MAN. CY.-S., SMC-3(6), 610-621, doi:10.1109/TSMC.1973.4309314, 1973.

Hersbach, H., Stoffelen, A., and de Haan, S.: An improved C-band scatterometer ocean geophysical model function: CMOD5, J. Geophys. Res., 112, C03006, doi:10.1029/2006JC003743, 2007.

Heinrichs, J. F., Cavalieri, D. J., and Markus, T.: Assessment of the AMSR-E sea ice concentration product at the ice edge using RADARSAT-1 and MODIS imagery, IEEE T. Geosci. Remote, 44(11), 3070-3080, doi: 10.1109/TGRS.2006.880622, 2006.

Ho, T. K.: The random subspace method for constructing decision forests, IEEE T. Pattern Anal., 20(8), 832-844, doi:10.1109/34.7096011998, 1998.

Isleifson, D., Galley, R. J., Barber, D. G., Landy, J. C., Komarov, A. S., and Shafai, L.: A study on the C-band polarimetric scattering and physical characteristics of frost flowers on experimental sea ice," IEEE T. Geosci. Remote, 52(3), 1787-1798, doi:10.1109/TGRS.2013.2255060, 2014.

JCOMM (Joint WMO-IOC Technical Commission for Oceanography and Marine Meteorology): Ice chart colour code standard, JCOMM Technical Report No. 24, Tech. rep., World Meteorological Organization, Geneva, Switzerland, 2014a.

JCOMM (Joint WMO-IOC Technical Commission for Oceanography and Marine Meteorology): SIGRID-3: a vector archive format for sea ice georeferenced information and data, JCOMM Technical Report No. 23, Tech. rep., World Meteorological Organization, Geneva, Switzerland, 2014b.

Johannessen, O.M., Alexandrov, V., Frolov, I.Y., Sandven, S., Pettersson, L.H., Bobylev, L.P., Kloster, K., Smirnov, V.G., Mironov, Y.U., and Babich, N.G.: Remote sensing of sea ice in the Northern Sea route: Studies and applications, Springer, Berlin, Heidelberg, doi:10.1007/978-3-540-48840-8, 2006.

Karvonen, J.: A sea ice concentration estimation algorithm utilizing radiometer and SAR data. The Cryosphere, 8, 1639-1650, doi:10.5194/tc-8-1639-2014, 2014.

Karvonen, J., Vainio, J., Marnela, M., Eriksson, P., and Niskanen, T.: A comparison between high-resolution EO-based and ice analyst-assigned sea ice concentrations, IEEE J. Sel. Top. Appl., 8(4), 1799-1807, 2015.

Karvonen, J.: Baltic sea ice concentration estimation using Sentinel-1 SAR and AMSR2 microwave radiometer data, IEEE T. Geosci. Remote, 55(5), 2871-2883, doi:10.1109/TGRS.2017.2655567, 2017.

Keller, M. R., Gifford, C. M., Walton, W. C., and Winstead, N. S.: Ice analysis based on active and passive radar images, U.S. Patent 9652674 B2, May 16, 2017. Available at: https://patents.google.com/patent/US9652674

Kohavi, R.: A Study of cross-validation and bootstrap for accuracy estimation and model selection, Proceedings of the 14th international joint conference on Artificial intelligence, Montreal, Canada, 20-25 August,1995, 2, 1137-1143, 1995.

Leigh, S., Wang, Z., and Clausi, D. A.: Automated ice-water classification using dual polarization SAR satellite imagery, IEEE T. Geosci. Remote, 52(9), 5529–5539, doi:10.1109/TGRS.2013.2290231, 2014.

Liu, H., Guo, H., and Zhang, L.: SVM-based sea ice classification using textural features and concentration from RADARSAT-2 dual-pol ScanSAR data, IEEE J. Sel. Top. Appl., 8(4), 1601–1613, doi:10.1109/JSTARS.2014.2365215, 2015.

Louppe, G.: Understanding random forests: From theory to practice, PhD Thesis, U. of Liege, 2014.

Mahmud, M. S., Geldsetzer, T., Howell, S. E. L., Yackel, J. J., Nandan, V., and Scharien, R. K.: Incidence angle dependence of HH-polarized C- and L-band wintertime backscatter over Arctic sea ice, IEEE T. Geosci. Remote, 56(11), 6686-6698, doi: 10.1109/TGRS.2018.2841343, 2018.

Mäkynen, M. and Karvonen, J.: Incidence angle dependence of first-year sea ice backscattering coefficient in Sentinel-1 SAR imagery over the Kara Sea, IEEE T. Geosci. Remote, 55(11), 6170-6181, doi:10.1109/TGRS.2017.2721981, 2017.

Mäkynen, M. P., Manninen, A. T., Simila, M. H., Karvonen, J. A., and Hallikainen, M. T.: Incidence angle dependence of the statistical properties of C-band HH-polarization backscattering signatures of the Baltic Sea ice, IEEE T. Geosci. Remote, 40(12), 2593-2605, doi:10.1109/TGRS.2002.806991, 2002.

Miranda, N.: S-1 constellation product performance status, SeaSAR 2018, Frascati, Italy, 7-10 May 2018. Available at: http://seasar2018.esa.int/files/presentation216.pdf

Park, J.-W., Korosov, A. A., Babiker, M., Sandven, S., and Won, J.-S.: Efficient thermal noise removal for Sentinel-1 TOPSAR cross-polarization channel, IEEE T. Geosci. Remote, 56(3), 1555–1565, doi:10.1109/TGRS.2017.2765248, 2018.

Park, J.-W., Won, J.-S., Korosov, A. A., Babiker, M., and Miranda, N.: Textural noise correction for Sentinel-1 TOPSAR cross-polarization channel images, IEEE T. Geosci. Remote, 57(6), 4040-4049, doi:10.1109/TGRS.2018.2889381, 2019.

Partington, K., Flynn, T., Lamb, D., Bertoia, C., and Dedrick, K: Late twentieth century Northern Hemisphere sea-ice record from the U.S. National Ice Center ice charts, J. Geophys. Res., 108(C11), doi:10.1029/2002JC001623, 2003.

Pastusiak, T.: Accuracy of sea ice data from remote sensing methods, its impact on safe speed determination and planning of voyage in ice-covered areas, International Journal on Marine Navigation and Safety of Sea Transportation, 10(2), 229-248, doi:10.12716/1001.10.02.06, 2016.

Pedregosa, F., Varoquaux, G., Gramfort, A., Michel, V., Thirion, B., Grisel, O., Blondel, M., Prettenhofer, P., Weiss, R., Dubourg, V., Vanderplas, J., Passos, A., Cournapeau, D., Brucher, M., Perrot, M., and Duchesnay, E.: Scikit-learn: Machine learning in Python, J. Mach. Learn. Res., 12, 2825-2830, doi:10.1016/j.patcog.2011.04.006, 2011.

Ressel, R., Frost, A., and Lehner, S.: A neural network-based classification for sea ice types on X-band SAR images, IEEE J. Sel. Top. Appl., 8(7), 3672-3680, doi:10.1109/JSTARS.2015.2436993, 2015.

Richards, F. J.: A flexible growth function for empirical use, J. Exp. Bot., 10(29), 290-300, doi: 10.1093/jxb/10.2.290, 1959.

Scheuchl, B., Flett, D., Caves, R., and Cumming, I.: Potential of RADARSAT-2 data for operational sea ice monitoring, Can. J. Remote Sens., 30(3), 448-471, 2004.

Shokr, M. E.: Evaluation of second-order texture parameters for sea ice classification from radar images, J. Geophys. Res.-Oceans, 96(C6), 10625-10640, 1991.

Smedsrud, L. H., Halvorsen, M. H., Stroeve, J. C., Zhang, R., and Kloster, K.: Fram Strait sea ice export variability and September Arctic sea ice extent over the last 80 years, The Cryosphere, 11, 65-79, doi:10.5194/tc-11-65-2017, 2017.

Soh, L.-K. and Tsatsoulis, C.: Texture analysis of SAR sea ice imagery using gray level co-occurrence matrices, IEEE T. Geosci. Remote, 37(2), 780-795, doi:10.1109/36.752194, 1999.

Wang, L., Scott, K. A., and Clausi, D. A., Sea ice concentration estimation during freeze-up from SAR imagery using a convolutional neural network, Remote Sens-Basel, 9(5), doi:10.3390/rs9050408, 2017.

Zakhvatkina, N. Y., Alexandrov, V. Y., Johannessen, O. M., Sandven, S., and Frolov, I. Y.: Classification of sea ice types in ENVISAT synthetic aperture radar images, IEEE T. Geosci. Remote, 51(5), 2587-2600, doi:10.1109/TGRS.2012.2212445, 2013.

Zakhvatkina, N., Korosov, A., Muckenhuber, S., Sandven, S., and Babiker, M.: Operational algorithm for ice-water classification on dual-polarized RADARSAT-2 images, The Cryosphere, 11, 33-46, doi:10.5194/tc-11-33-2017, 2017.

Figures

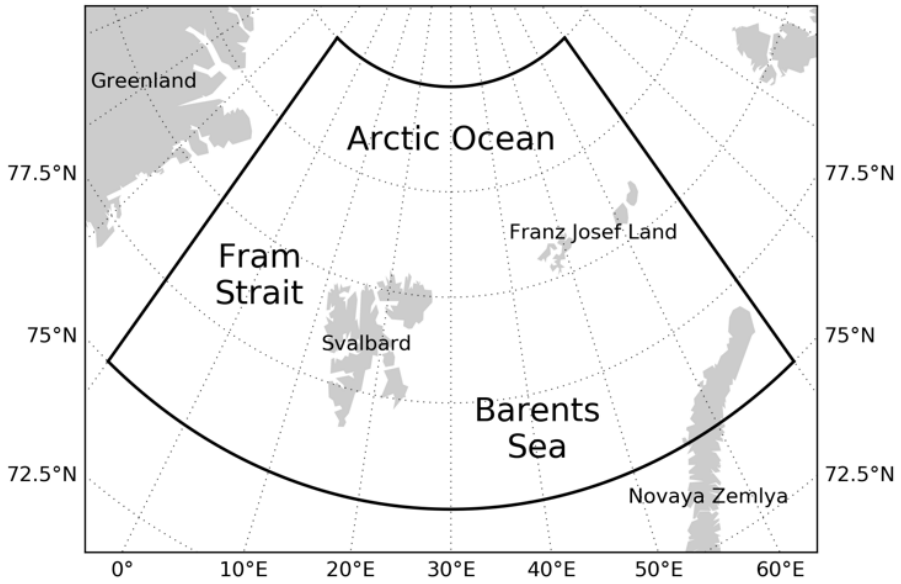

Figure 1: Study area.

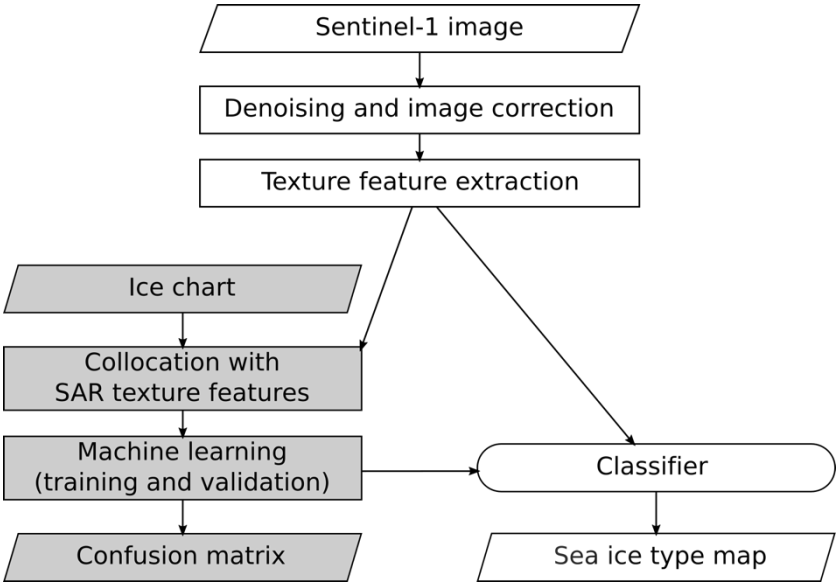

Figure 2: Processing flowchart of the proposed algorithm. The gray color shows the training phase.

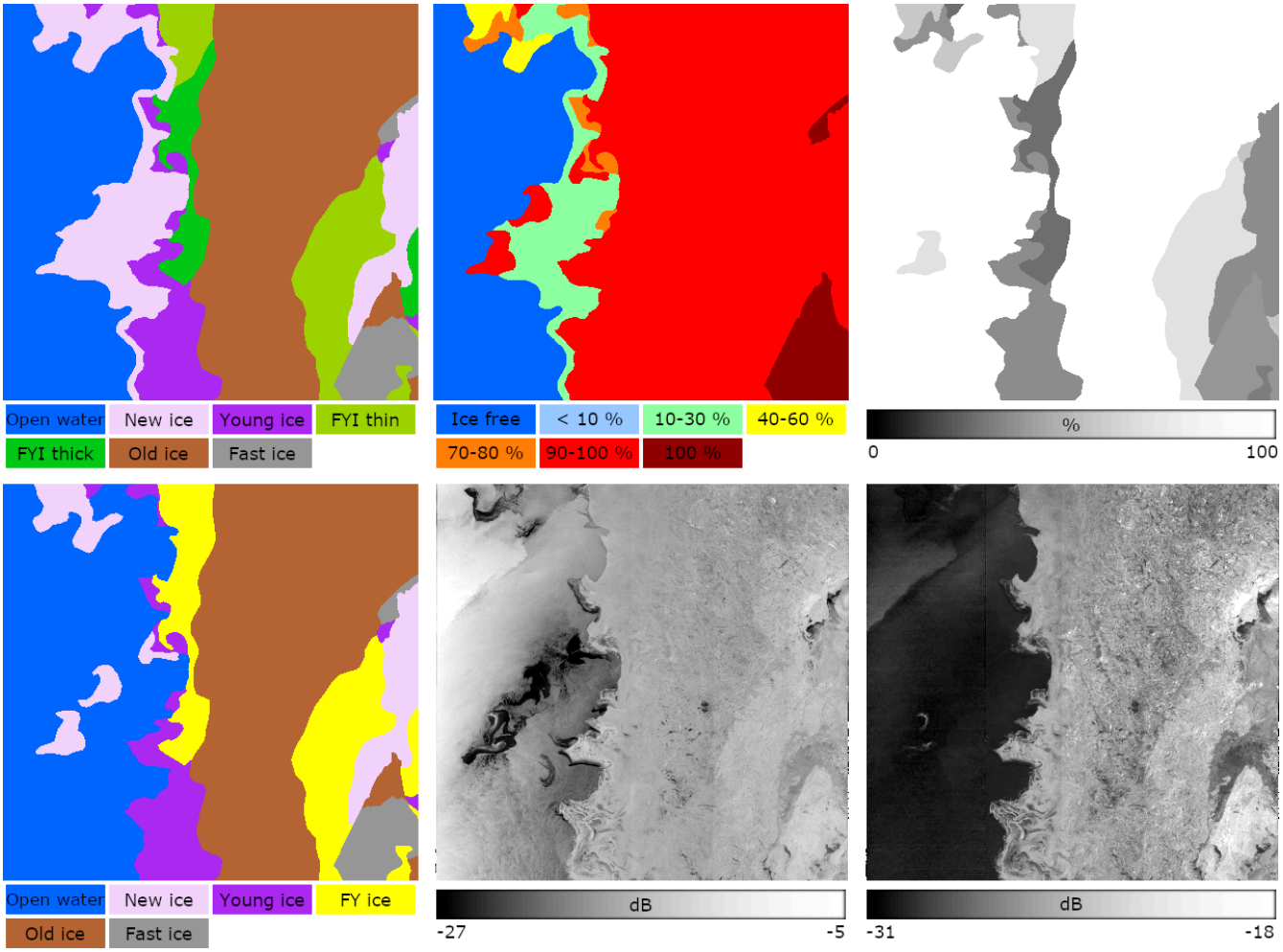

Figure 3: An example of the ice chart preprocessing. From the ice chart, stage of development (SoD; Top left), ice concentration (CT; Top center), and partial concentration of the dominant ice type (CP; Top right) maps are extracted. Then, some of the different SoDs are merged (e.g., thin and thick first-year ices are merged into a single label as first-year ice) and the area with low ice concentration is labeled as open water. The processed map of SoD (Bottom left) is related with textural features extracted from HH and HV polarization images (Bottom center and bottom right). Note that the NIC ice chart which was published on January 25, 2018, and the Sentinel-1 product S1B_EW_GRDM_1SDH_20180122T075237_20180122T075337_009281_010A4D_65AA acquired over the Fram Strait were used in this example.

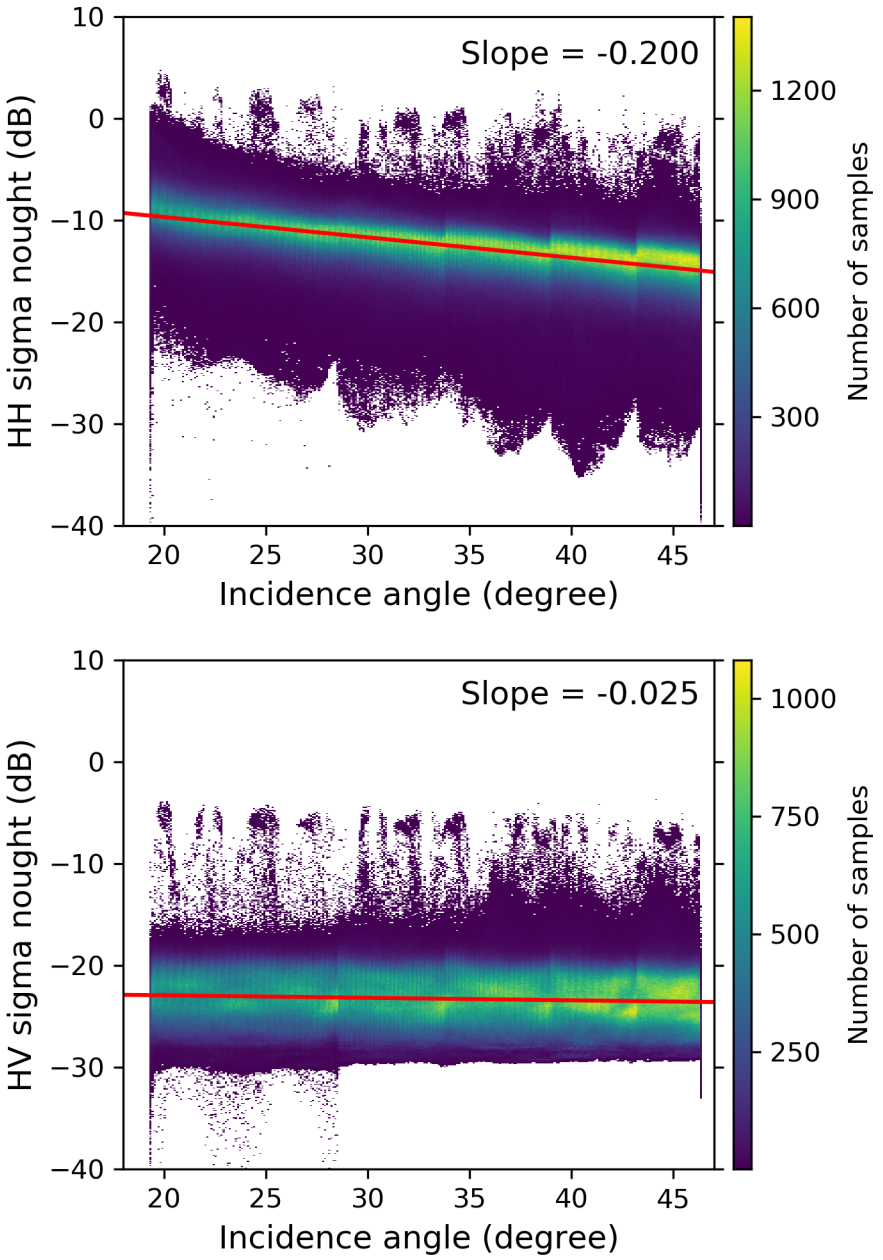

Figure 4: Two-dimensional histograms of incidence angle versus sigma nought for HH (top) and HV (bottom) polarization channels. Pixels covering various types of sea ice were merged so that the averaged property can be estimated. The best fit linear trends are shown with red lines.

5

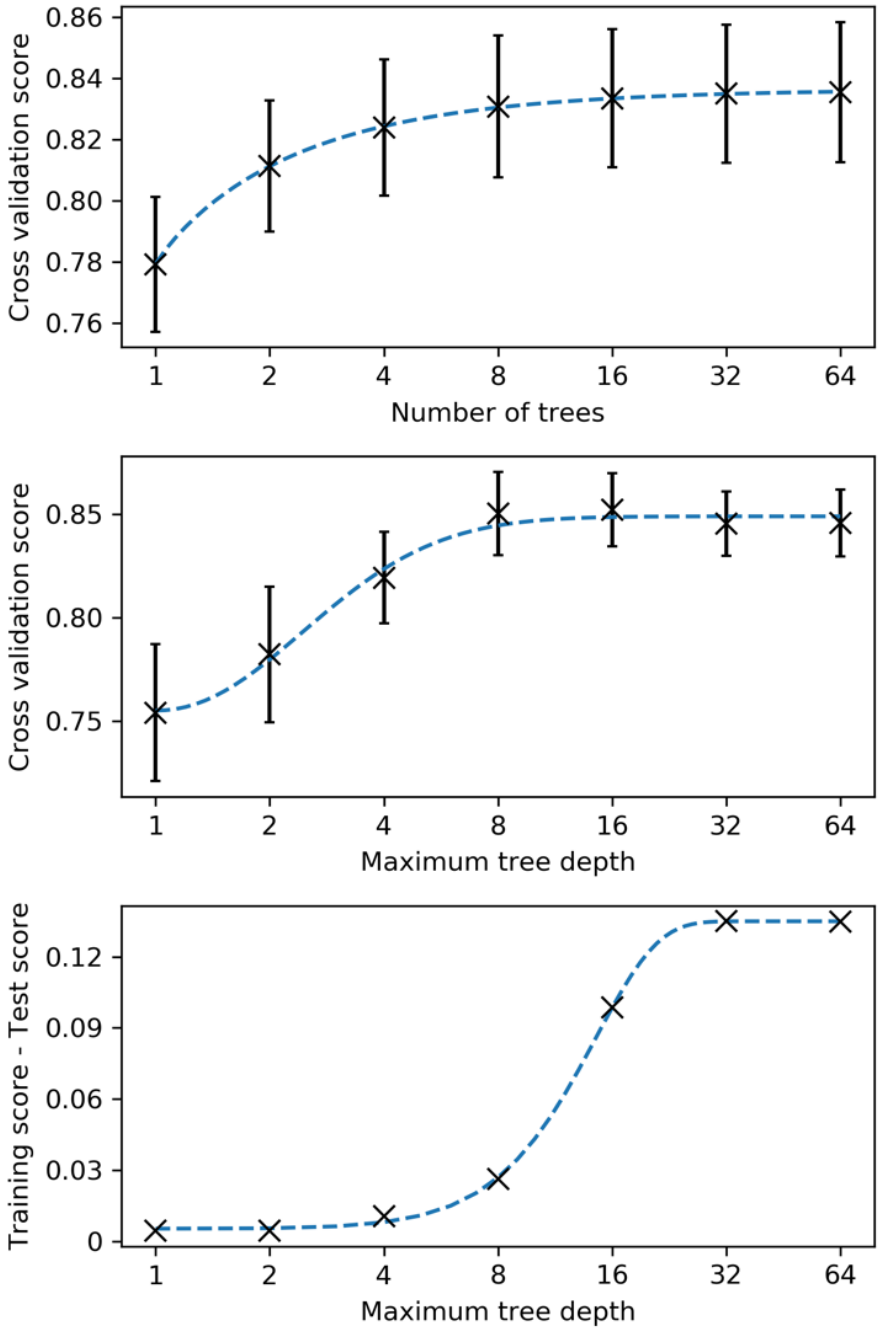

Figure 5: Hyperparameter optimization using grid search results (cross). Dashed lines represent the best-fit Richards' Curve. (Top panel) The optimal values are extracted from the locations where the score increments per unit of each hyperparameter become lower than a threshold (e.g., 0.001). (Center panel) If the curve does not fit the grid search results well, (Bottom panel) the difference between training and test scores is used to find the locations where it does not exceed a threshold (e.g., 0.03) in order to avoid overfitting.

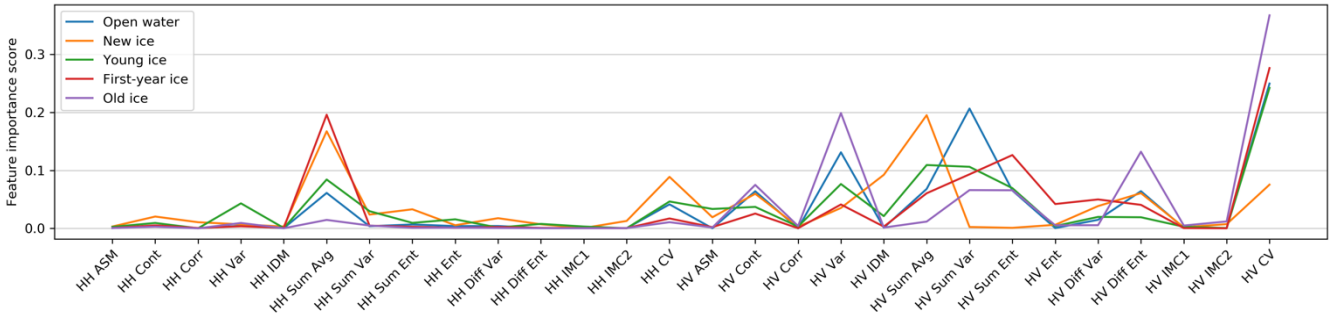

Figure 6: Feature importances of the binary sub-classifiers. ASM: angular second moment; Cont: contrast; Corr: correlation; Var: variance; IDM: inverse difference moment; Sum Avg: sum average; Sum Var: sum variance; Sum Ent: sum entropy; Ent: entropy; Diff Var: difference variance; Diff Ent: difference entropy; IMC: information measures of correlation; CV: coefficient of variation. For definitions of each parameters, please refer to Haralick et al., 1973.

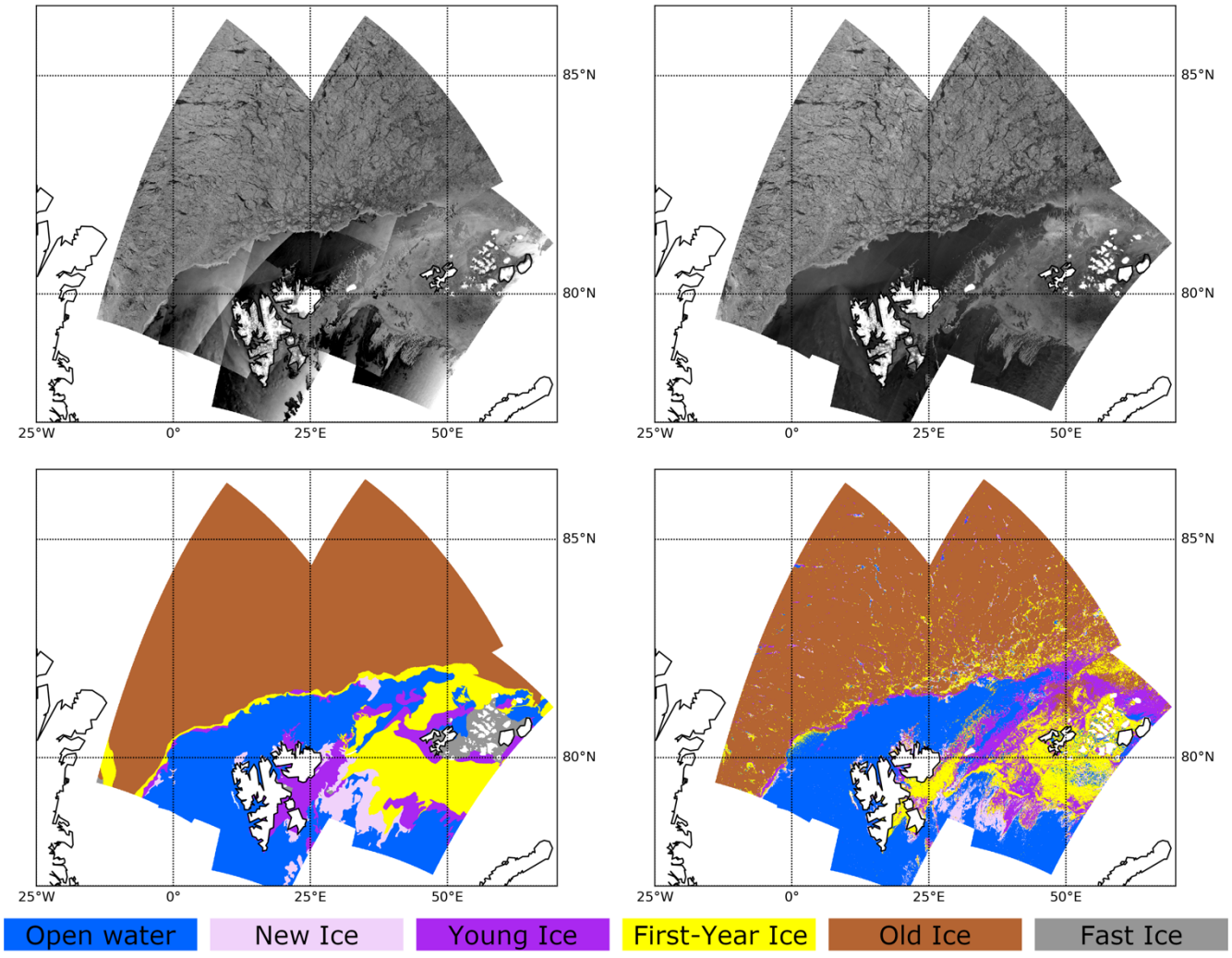

Figure 7: One-day mosaics of Sentinel-1A/1B images (Top left: HH, Top right: HV) and the ice classification result (Bottom right) on 5 February 2019. The publication date of the reference weekly ice chart is 8 February 2019 (Bottom left).

5

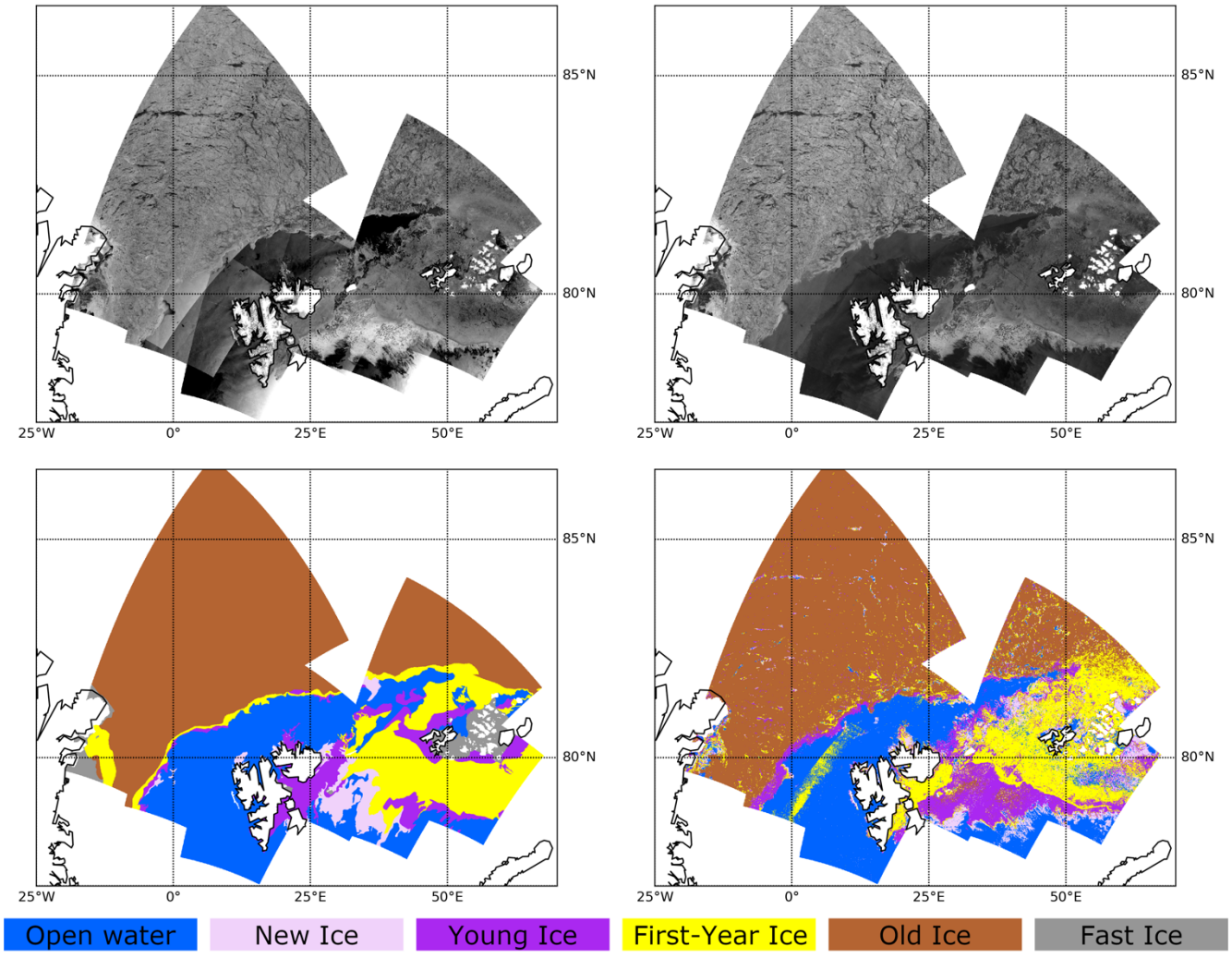

Figure 8: One-day mosaics of Sentinel-1A/1B images (Top left: HH, Top right: HV) and the ice classification result (Bottom right) on 8 February 2019. The publication date of the reference weekly ice chart is 8 February 2019 (Bottom left).

5

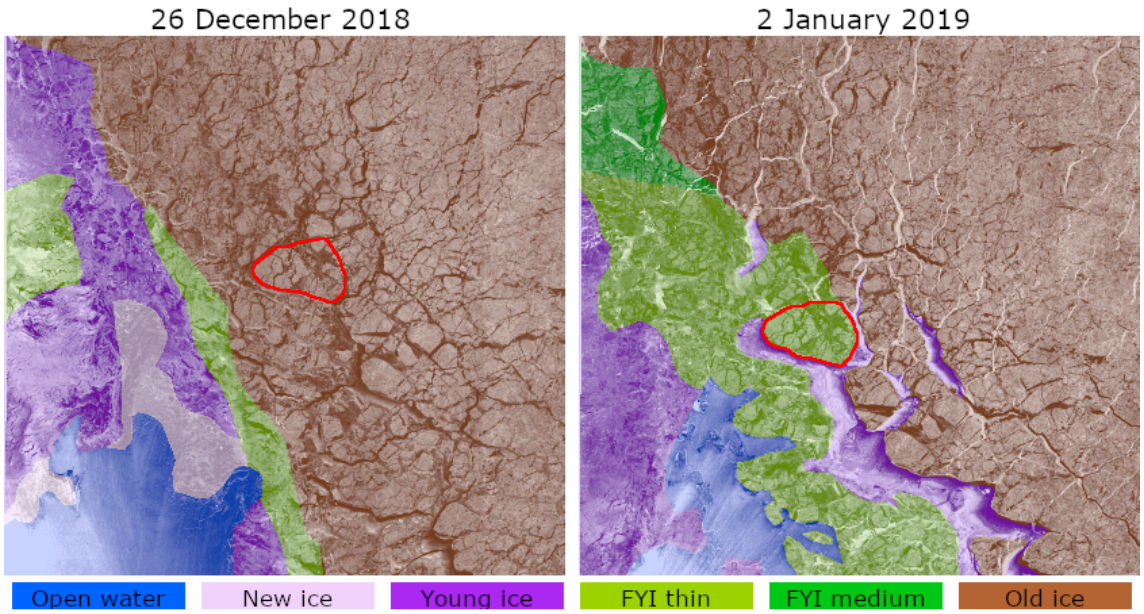

Figure 9: An example of the inconsistency of the ice charts. The SoDs from the NIC ice charts on different dates (26 December 2018 and 2 January 2019) are superimposed on the Sentinel-1 backscattering image of the corresponding dates. The same ice floe (red outline) is classified differently in each ice chart (old ice on the left panel and first-year ice on the right panel) despite of the similarity in the SAR backscattering images.

Tables

Table 1: Hyperparameters used for grid search

Parameters	Values						
N_T	1	2	4	8	16	32	64
D	1	2	4	8	16	32	64
N_F	1	2	4	8	16	28	

Table 2: Confusion matrix of the five-class RF classifier which was trained with and applied to the 2018 dataset

		Predicted														
		OW (open water)			NI (new ice)			YI (young ice)			FYI (first-year ice)			OI (old ice)		
	case	FC1	FC2	FC3	FC1	FC2	FC3	FC1	FC2	FC3	FC1	FC2	FC3	FC1	FC2	FC3
Actual	OW	**94.5**	**95.2**	**96.7**	1.4	1.1	0.6	0.3	0.3	0.3	3.7	3.4	2.4	0.0	0.0	0.0
	NI	19.3	17.3	14.8	**33.1**	**38.9**	**68.7**	33.3	31.1	9.3	12.1	10.6	5.5	2.2	2.1	1.7
	YI	1.9	1.8	1.6	3.8	3.6	6.7	**62.3**	**62.8**	**64.5**	26.1	27.5	23.8	5.9	4.3	3.4
	FYI	4.2	3.6	2.4	2.6	2.6	2.1	21.7	20.6	15.6	**58.1**	**61.1**	**69.8**	13.4	12.1	10.1
	OI	0.3	0.3	0.4	0.6	0.8	1.4	5.8	5.0	3.0	7.3	7.3	4.1	**86.0**	**86.7**	**91.2**

Table 3: Confusion matrix of the five-class RF classifier which was trained with 2018 dataset and applied to the 2019 dataset

		Predicted														
		OW (open water)			NI (new ice)			YI (young ice)			FYI (first-year ice)			OI (old ice)		
	case	FC1	FC2	FC3	FC1	FC2	FC3	FC1	FC2	FC3	FC1	FC2	FC3	FC1	FC2	FC3
Actual	OW	**90.1**	**90.6**	**85.4**	3.1	2.7	5.7	1.0	1.1	2.0	5.8	5.7	6.9	0.0	0.0	0.0
	NI	20.1	24.5	28.3	**28.0**	**23.0**	**23.9**	42.0	42.4	40.9	7.6	7.9	5.5	2.4	2.1	1.4
	YI	6.7	6.1	6.3	3.3	3.4	3.1	**44.7**	**44.6**	**51.5**	36.0	38.2	33.5	9.3	7.7	5.7
	FYI	5.4	4.4	4.9	3.6	3.8	2.7	25.8	25.3	27.5	**38.9**	**42.0**	**46.0**	26.3	24.5	18.9
	OI	0.5	0.5	0.5	1.3	1.2	0.7	2.7	3.0	7.7	2.8	3.6	24.9	**92.7**	**91.7**	**66.3**

Table 4: Classification accuracies before and after applying textural denoising

class	case								
	FC1			FC2			FC3		
	Thermal denoising only	Textural denoising applied	difference	Thermal denoising only	Textural denoising applied	difference	Thermal denoising only	Textural denoising applied	difference
OW	88.4	90.1	+1.7	88.9	90.6	+1.7	88.0	85.4	-2.6
NI	30.2	28.0	-2.8	27.7	23.0	-4.7	31.8	23.9	-7.9
YI	34.9	44.7	+9.8	36.2	44.6	+8.2	43.4	51.5	+8.1
FYI	29.3	38.9	+9.6	30.4	42.0	+11.6	38.0	47.0	+9.0
OI	91.5	92.7	+1.2	90.3	91.7	+1.4	75.2	66.3	-8.9
kappa	0.62	0.67	+0.05	0.62	0.67	+0.05	0.54	0.49	-0.05

Table 5: Confusion matrix of the three-class RF classifier which were trained and applied to the 2018 dataset

		Predicted								
		OW (open water)			mFYI (mixed FYI)			OI (old ice)		
	Case	FC1	FC2	FC3	FC1	FC2	FC3	FC1	FC2	FC3
Actual	OW	**96.7**	**97.3**	**99.1**	3.3	2.6	0.9	0.0	0.0	0.0
	mFYI	5.2	4.7	2.5	**85.8**	**87.6**	**92.3**	9.0	7.7	5.2
	OI	0.4	0.4	0.2	13.2	12.4	6.0	**86.4**	**87.2**	**93.8**

Table 6: Confusion matrix of the three-class RF classifier which was trained with the 2018 dataset and applied to the 2019 dataset

		Predicted								
		OW (open water)			mFYI (mixed FYI)			OI (old ice)		
	Case	FC1	FC2	FC3	FC1	FC2	FC3	FC1	FC2	FC3
Actual	OW	**93.6**	**93.6**	**86.3**	6.4	6.4	13.6	0.0	0.0	0.0
	mFYI	8.8	7.5	7.1	**72.4**	**75.3**	**81.6**	18.8	17.2	11.3
	OI	0.6	0.6	0.4	6.7	8.1	39.8	**92.7**	**91.4**	**59.7**